ORIGINAL PAPER

Glenn A. Gaetani · Adam J. R. Kent
Timothy L. Grove · Ian D. Hutcheon
Edward M. Stolper

Mineral/melt partitioning of trace elements during hydrous peridotite partial melting

Abstract This experimental study examines the mineral/melt partitioning of incompatible trace elements among high-Ca clinopyroxene, garnet, and hydrous silicate melt at upper mantle pressure and temperature conditions. Experiments were performed at pressures of 1.2 and 1.6 GPa and temperatures of 1,185 to 1,370 °C. Experimentally produced silicate melts contain up to 6.3 wt% dissolved H_2O, and are saturated with an upper mantle peridotite mineral assemblage of olivine + orthopyroxene + clinopyroxene + spinel or garnet. Clinopyroxene/melt and garnet/melt partition coefficients were measured for Li, B, K, Sr, Y, Zr, Nb, and select rare earth elements by secondary ion mass spectrometry. A comparison of our experimental results for trivalent cations (REEs and Y) with the results from calculations carried out using the Wood-Blundy partitioning model indicates that H_2O dissolved in the silicate melt has a discernible effect on trace element partitioning. Experiments carried out at 1.2 GPa, 1,315 °C and 1.6 GPa, 1,370 °C produced clinopyroxene containing 15.0 and 13.9 wt% CaO, respectively, coexisting with silicate melts containing ∼1–2 wt% H_2O. Partition coefficients measured in these experiments are consistent with the Wood-Blundy model. However, partition coefficients determined in an experiment carried out at 1.2 GPa and 1,185 °C, which produced clinopyroxene containing 19.3 wt% CaO coexisting with a high-H_2O (6.26 ± 0.10 wt%) silicate melt, are significantly smaller than predicted by the Wood-Blundy model. Accounting for the depolymerized structure of the H_2O-rich melt eliminates the mismatch between experimental result and model prediction. Therefore, the increased Ca^{2+} content of clinopyroxene at low-temperature, hydrous conditions does not enhance compatibility to the extent indicated by results from anhydrous experiments, and models used to predict mineral/melt partition coefficients during hydrous peridotite partial melting in the sub-arc mantle must take into account the effects of H_2O on the structure of silicate melts.

G. A. Gaetani (✉) · T. L. Grove
Department of Earth,
Atmospheric and Planetary Sciences,
Massachusetts Institute of Technology,
Cambridge, MA, 02139, USA
E-mail: ggaetani@whoi.edu

G. A. Gaetani · A. J. R. Kent · E. M. Stolper
Division of Geological and Planetary Sciences,
California Institute of Technology,
Pasadena, CA, 91125, USA

G. A. Gaetani
Department of Geology and Geophysics,
Woods Hole Oceanographic Institution,
Woods Hole, MA, 02543, USA

A. J. R. Kent · I. D. Hutcheon
Analytical and Nuclear Chemistry Division,
Lawrence Livermore National Laboratory,
Livermore, CA, 94551, USA

Present address: A. J. R. Kent
Department of Geosciences,
Oregon State University, Corvallis,
OR, 97331-5506, USA

Introduction

Trace element and isotopic studies of subduction-related volcanic rocks play a prominent role in guiding our understanding of melt generation in the sub-arc mantle. Subduction-related lavas are typically enriched in the large ion lithophile elements (LILEs; e.g., Sr, K, Ba, U, Th) and depleted in the high field strength elements (HFSEs; e.g., Ti, Zr, Nb, Hf) relative to mid-ocean ridge basalts (MORB). This trace element pattern has been interpreted as resulting from metasomatism of peridotite in the sub-arc mantle, prior to partial melting, by an H_2O-rich component derived from the subducting oceanic lithosphere (e.g., Perfit et al. 1980; Arculus and Johnson 1981; Maury et al. 1992). In addition to enriching the mantle wedge in incompatible trace

elements, this subduction component is thought to initiate partial melting at temperatures well below the anhydrous mantle solidus through fluxing of the peridotite (e.g., Gill 1981; Wyllie 1982; Davies and Stevenson 1992; Stolper and Newman 1994). Therefore, the development of forward models to describe the behavior of trace elements in the subducting lithosphere and mantle wedge requires experimental determinations of both mineral/aqueous fluid and mineral/hydrous silicate melt partition coefficients at temperature and pressure conditions comparable to those in the sub-arc mantle.

Mineral/aqueous fluid partition coefficients have been experimentally determined for eclogite–, peridotite–, and sediment–H_2O systems (e.g., Schneider and Eggler 1986; Tatsumi et al. 1986; Brenan and Watson 1991; Brenan et al. 1994; Ayers and Eggler 1995; Brenan et al. 1995a, 1995b; Ayers et al. 1997; Johnson and Plank 1999). Here we present an experimental determination of mineral/melt partition coefficients for incompatible trace elements during partial melting of hydrous peridotite at conditions relevant to the sub-arc mantle. The data show that, for example, rare earth elements are not as compatible under hydrous conditions as would be predicted on the basis of the composition of the clinopyroxene (Cpx). This result demonstrates that the low degree of polymerization of hydrous partial melts significantly affects trace element partitioning. Therefore, models designed to predict the partitioning of trace elements between Cpx and anhydrous silicate melt cannot be used to quantify melt generation under hydrous conditions in the sub-arc mantle.

Experimental and analytical methods

Experimental methods

Experiments were performed by melting mixtures of natural basalt and synthetic peridotite, using a 1.27-cm solid-medium piston cylinder device (Boyd and England 1960). Experiments were pressurized to 1.0 GPa at room temperature, heated to 865 °C at 100 °C/min, then taken to the experimental pressure and held for 6 min. Temperature was then increased at 50 °C/min until the desired experimental conditions were achieved. The pressure medium consisted of sintered $BaCO_3$ which was found to have a friction correction of 300 MPa through calibration against the pressure-dependent melting point of Au (Akella and Kennedy 1971), and the Ca-Tschermakite breakdown reaction (Hays 1966). This correction has been applied to the pressures reported in Table 1, which are thought to be accurate to within ± 50 MPa. Temperature was monitored and controlled using $W_{97}Re_3$–$W_{75}Re_{25}$ thermocouples, with no correction for the effect of pressure on thermocouple EMF. A temperature difference of 20 °C was measured between the location of the thermocouple junction and the furnace hotspot, using offset thermocouples. The temperatures reported in Table 1 have been corrected for this difference. Temperatures are thought to be accurate to within ± 10 °C.

High-H_2O ($\sim$5–6 wt% in the glass) melting experiments were prepared by packing $\sim$15 mg of powder into a capsule fabricated from $Au_{90}Pd_{10}$ alloy which had been conditioned to minimize Fe loss from the silicate, and welding it shut. The sealed inner capsule

Table 1 Summary of experimental conditions and products

Experiment	B287			B329			B394			B366		
P (GPa)	1.2			1.2			1.6			1.6		
T (°C)	1,315			1,185			1,370			1,230		
Melt (wt%)	58.6(11)			59.0(15)			64.1(15)			56.5(26)		
H_2O in melt (wt%)	0.98(24)			6.26(10)			1.70(17)			4.8(6)		
Duration (h)	24			26			24			22		
Run products	Gl, Cpx, Opx, Oliv, Sp			Gl, Cpx, Opx, Oliv, Sp			Gl, Cpx, Opx, Oliv, Sp			Gl, Cpx, Opx, Oliv, Gt		
	Gl	Cpx	D_i	Gl	Cpx	D_i	Gl	Cpx	D_i	Gl	Gt	D_i
Li	2.06(18)	0.71(16)	0.34(8)	2.23(14)	0.59(6)	0.26(3)	–	–	–	2.2(3)	0.043(17)	0.020(8)
B	41.2(15)	2.4(7)	0.058(17)	36(2)	2.9(7)	0.08(2)	–	–	–	21.53(19)	0.07(4)	0.0033(19)
Na	18,500(300)	4,160(60)	0.225(5)	17,100(300)	3,780(60)	0.221(5)	16,500(100)	4,670(60)	0.283(4)	–	–	–
K	1,000(30)	9(2)	0.009(2)	1,000(30)	1.3(3)	0.0013(3)	1,000(30)	6(1)	0.006(1)	900(30)	0.50(25)	0.0006(3)
Ti	3,960(60)	1,500(80)	0.38(2)	3,780(40)	1,200(50)	0.32(1)	3,600(60)	1,200(60)	0.33(2)	3,960(60)	1,100(100)	0.28(3)
Sr	166(4)	15(3)	0.09(2)	175(7)	22(3)	0.13(2)	185(25)	28(4)	0.15(3)	180(17)	1.1(6)	0.006(3)
Y	16(1)	10(1)	0.63(9)	16(2)	10(1)	0.63(10)	19(2)	10.4(11)	0.55(8)	11.0(11)	45(4)	4.1(5)
Zr	41(3)	6(1)	0.15(3)	41(4)	7.1(9)	0.17(3)	44(5)	6.6(10)	0.15(3)	36(5)	17(2)	0.47(9)
Nb	–	–	–	–	–	–	–	–	–	1.6(4)	0.08(3)	0.05(2)
La	1.60(15)	0.13(4)	0.09(3)	1.69(19)	0.17(9)	0.10(5)	1.7(3)	0.16(5)	0.09(3)	–	–	–
Ce	4.4(7)	0.51(11)	0.12(3)	4.4(4)	0.69(19)	0.16(5)	4.8(6)	0.63(11)	0.13(3)	4.8(6)	0.05(3)	0.010(6)
Nd	4.1(2)	0.93(13)	0.23(3)	4.5(3)	1.2(3)	0.27(7)	4.5(3)	1.15(13)	0.26(3)	4.2(3)	0.30(6)	0.071(15)
Sm	1.45(18)	0.52(12)	0.36(9)	1.6(2)	0.7(3)	0.44(17)	1.7(2)	0.64(12)	0.38(8)	1.50(19)	0.51(10)	0.34(8)
Eu	0.62(8)	0.16(4)	0.26(8)	0.70(13)	0.27(11)	0.39(18)	0.74(12)	0.18(5)	0.24(8)	0.66(9)	0.29(5)	0.44(10)
Dy	2.6(3)	1.6(4)	0.62(17)	2.6(5)	2.0(9)	0.77(36)	3.0(7)	1.7(4)	0.57(19)	2.0(4)	6.4(16)	3.2(10)
Er	1.85(20)	1.3(3)	0.70(16)	1.8(3)	1.3(6)	0.72(34)	2.2(4)	1.3(3)	0.59(17)	1.2(2)	6(2)	5.0(19)
Yb	2.09(15)	1.43(16)	0.68(9)	2.0(2)	1.2(3)	0.62(14)	2.32(19)	1.41(15)	0.61(8)	1.08(11)	8.0(8)	7.4(11)

Concentrations are reported in parts per million unless specified otherwise. Units in parentheses are 1σ uncertainties in terms of least units cited. Thus, 0.61(8) should be read as 0.61 ± 0.08

was then placed into a graphite sleeve which was, in turn, placed into an outer capsule made from $Au_{80}Pt_{20}$ alloy. Graphite powder was then packed into the outer capsule, and it was welded shut. The sealed outer capsule was placed into a high-density Al_2O_3 sleeve and centered in the hotspot of a straight-walled graphite furnace, using crushable MgO spacers. Low-H_2O ($\sim$1–2 wt% in the glass) experiments were prepared by packing $\sim$6 mg of powder into a graphite crucible and placing a graphite lid on top. The crucible was then placed into a Pt capsule, and held at 120 °C in a drying oven for 16 to 21 h. Upon removal from the oven, dried graphite powder was packed on top of the crucible lid and the Pt capsule was welded shut. The sealed outer capsule was then placed into an assembly identical to that used for the high-H_2O experiments. Additional details regarding starting materials and experimental techniques are given by Gaetani and Grove (1998).

Analytical methods

The major element compositions of all experimental run products were determined using either a 4- or 5-spectrometer JEOL 733 electron microprobe at the Massachusetts Institute of Technology. A 10-nA beam current and 15-kV accelerating voltage were used for all analyses. Beam diameters were 10 or 20 μm for glass, and 2 μm for crystals. Online data reduction was accomplished using the phi-rho-z correction scheme. Migration of Na during the analysis of hydrous glasses was minimized through use of a 20-μm beam and by measuring Na for 5 s prior to determination of the other elements, which had maximum peak counting times of 40 s (Sisson and Grove 1993). Replicate analyses of an experimentally produced basaltic glass were used to estimate analytical precision. Standard deviations calculated on the basis of the distribution of 390 analyses performed over 37 months expressed as percent relative are as follows: 0.52% for SiO_2, 0.90% for Al_2O_3, 0.98% for CaO, 1.3% for MgO, 2.1% for FeO, 5.0% for TiO_2, 6.5% for Na_2O, 6.7% for K_2O, 31% for MnO, 38% for Cr_2O_3, and 65% for P_2O_5. The mean sum for the 390 analyses is 99.98 wt%.

The H_2O contents of the experimentally produced glasses were determined either by Fourier transform infrared (FTIR) spectroscopy at the California Institute of Technology (B287), or by secondary ion mass spectrometry (SIMS) using either the modified Cameca IMS 3f ion microprobe at Lawrence Livermore National Laboratory (B329; B366), or the Cameca IMS 6f ion microprobe at the Department of Terrestrial Magnetism (B394). Analytical procedures for the FTIR analyses followed the general methods of Dixon et al. (1991). The SIMS analyses carried out using the Cameca 3f followed the analytical procedures reported by Gaetani and Grove (1998) and by Kent et al. (1999), whereas the procedures of Hauri et al. (2002) were used for analyses done using the Cameca 6 f.

The concentrations of trace elements in glasses and crystals were measured using the modified Cameca IMS 3f ion microprobe at Lawrence Livermore National Laboratory. A 17-keV $^{16}O^-$ primary ion beam with 5- to 30-nA current, focused to a 25- to 40-μm diameter spot, was used to sputter material from crystals and glasses of interest. Positive secondary ions were extracted and accelerated, nominally to 4.5 keV. A field aperture inserted in the sample image plane allowed only ions from the central 30-μm diameter area of the imaged field to enter the mass spectrometer, using a mass resolving power of $\sim$600. Isobaric molecular interferences were minimized by energy filtering, using a 40-eV window and an offset of 80 V from the voltage at which the energy distribution of $^{16}O^+$ dropped to 10% of its maximum value on the low-energy side. Samples were coated with Au prior to analysis to reduce charge buildup, and periodic measurements of the energy distribution of $^{16}O^+$ and adjustments of the accelerating voltage to maintain a constant voltage offset further mitigated the effects of charging. The ion beam was rastered over a 100×100 μm area corresponding with the analysis location for $\sim$5 min in order to remove surface contamination prior to analysis (this was particularly important for boron analyses). Previous work shows that this approach effectively removes surface contamination associated with sample handling and coating (Kent et al. 1999).

Trace element analysis involved sequential scans of ^{7}Li, ^{11}B, ^{16}O, ^{30}Si, ^{42}Ca, ^{86}Sr, ^{89}Y, ^{90}Zr, ^{93}Nb, ^{138}Ba, ^{139}La, ^{140}Ce, ^{142}Ce, ^{143}Nd, ^{145}Nd, ^{146}Nd, ^{147}Sm, ^{148}Sm, ^{151}Eu, ^{152}Sm, ^{153}Eu, ^{154}Sm, ^{161}Dy, ^{162}Dy, ^{163}Dy, ^{166}Er, ^{167}Er, ^{168}Er, ^{171}Yb, ^{172}Yb, ^{173}Yb, and ^{174}Yb; integration times were 1 to 20 s, depending on intensity. Trace element concentrations were calculated from either ^{30}Si-normalized (garnet, Gt) or ^{42}Ca-normalized (glass and Cpx) ion intensities, using sensitivity factors determined from analysis of NBS 612 glass, and electron microprobe measurements of CaO for Cpx and glass and of SiO_2 for Gt. The isobaric interferences of light REE oxides on heavy REEs were corrected using the procedure outlined in Zinner and Crozaz (1986) and Fahey et al. (1987). The oxide-to-metal ($REEO^+/REE^+$) correction factors for Gd, Yb, and Lu were determined from measurement of LREE-doped Cpx glass standards (Kennedy and Hutcheon 1992).

The accuracy of the trace element measurements was evaluated through analysis of the basalt glass secondary standard, BHVO. The results show close agreement between measured and accepted values (Table 2), with the measured concentrations of all elements except Yb lying within $\sim$10% of the accepted values. Measured Yb values in BHVO are $\sim$30% higher than those reported by Govindaraju (1989). This discrepancy is not fully understood but most likely reflects an underestimate of the oxide-to-metal correction factor. Given the relatively large uncertainties associated with Yb concentrations measured in glass and crystals in this study, as well as partition coefficients derived from them, we made no attempt to apply a secondary correction to measured Yb concentrations.

Table 2 Measured trace element concentrations in BHVO standard glass

	Accepted concentration[a]	Aver. measured concentration	1 Standard deviation (%)[b]	Measured/ accepted
Sr	390	375	2.6	0.96
Y	27	26.3	2.1	0.98
Zr	180	186	4.0	1.03
Nb	19.5	17.5	7.8	0.89
Ba	133	121	8.1	0.91
La	15.5	14.2	5.4	0.91
Ce	38.0	35.9	6.8	0.95
Nd	24.7	24.8	5.1	1.00
Sm	6.17	6.2	7.2	1.00
Eu	2.06	2.1	5.3	1.01
Dy	5.25	5.6	14.9	1.07
Er	2.56	2.9	10.2	1.11
Yb	1.98	2.6	4.5	1.30

[a]From Govindaraju (1989)
[b]Average and standard deviation calculated from four analyses of BHVO glass over a two-month period. Note that Li and B were not measured in these analyses

No attempt was made to correct calculated B and Li concentrations for the effect of the lower ion sensitivities (with respect to ^{30}Si) observed in high-H_2O glasses by Brenan et al. (1998). The highest H_2O content in our experimentally produced glasses (6.3 wt%) is less than half of the 13.6 wt% H_2O dissolved in the glasses analyzed by Brenan et al. (1998), so that the depression of measured B and Li concentrations is likely to be, at most, on the order of ~15 and 6%, respectively. Although this will directly translate to lower measured partition coefficients for these elements, the magnitude of the change is within the uncertainty estimate on the B and Li partition coefficients.

Potassium contents of Cpx and Gt were analyzed separately from other trace elements on mineral grains which were the same as, or directly adjacent to, those analyzed previously. In order to resolve the isobaric interference from NaO (which is incompletely removed by energy filtering), K concentrations were analyzed at a mass resolving power of ~2,100 using a 5-nA primary beam and a field aperture with an effective diameter of 8 μm, with an energy offset of 10 ± 20 V. These analyses involved sequential measurement of ^{16}O, ^{30}Si, ^{39}K, and ^{42}Ca; measurements of NBS 610, 612 and 614 glasses and the ION-1 Cpx standard, containing 80 ppm K, from a garnet lherzolite were used to calibrate measured $^{39}K^+/^{30}Si^+$ ratios to K contents.

Uncertainties for measured REE concentrations reported in Table 1 were calculated from the standard deviations of ion intensity ratios from individual analyses. The accuracy of K analyses in Cpx and Gt is estimated at $\pm 15\%$ (1σ) on the basis of replicate measurements of the ION-1 Cpx standard. Uncertainties in the derived partition coefficients are the quadratic summation of individual uncertainties in elemental concentrations.

Experimental results

Experiments produced silicate melt saturated with an upper mantle peridotite mineral assemblage of olivine (Oliv) + orthopyroxene (Opx) + Cpx + spinel (Sp) or Gt (Table 1). Experimental charges contain 57–64 wt% quenched silicate melt, 12–17 wt% Cpx, 11–15 wt% Opx, 5–14 wt% Oliv, and either ~2 wt% Sp or ~12 wt% Gt, as determined by mass-balance calculations. Areas of quench-growth-free glass ~150 to 700 μm wide are present in each charge. Clinopyroxene grains are ~20 to 40 μm in diameter whereas Gt crystals are ~200 to 400 μm across, often poikilitically enclosing small pyroxenes. Detailed descriptions of the sizes and morphologies of the crystalline phases are given by Gaetani (1996).

Major element compositions of all experimentally produced phases are reported in Table 3. The quenched silicate melts have molar $Mg/(Mg + \Sigma Fe)$ ratios of 0.6990 ± 0.0014 to 0.7288 ± 0.0008, and incompatible minor element concentrations (0.60 ± 0.03 to 0.66 ± 0.03 wt% TiO_2; 2.22 ± 0.05 to 2.50 ± 0.11 wt% Na_2O; 0.11 ± 0.02 to 0.12 ± 0.01 wt% K_2O) comparable to those expected of peridotite partial melts (e.g., Presnall and Hoover 1987). Silicate melts produced in the high-H_2O experiments are characterized by low SiO_2, FeO*, and MgO relative to those from the low-H_2O experiments when H_2O is included in the melt composition (Fig. 1a). Mineral compositions are broadly similar to those expected in fertile mantle peridotite. The molar $Mg/(Mg + Fe)$ ratios of Oliv range from 0.8736 ± 0.0004 to 0.8945 ± 0.0003, Opx from

0.8801 ± 0.0004 to 0.8965 ± 0.0005, and Cpx from 0.8808 ± 0.0016 to 0.8889 ± 0.0014. At a given pressure, the compositions of coexisting pyroxenes which crystallize in the high-H_2O experiments differ from those in the low-H_2O experiments, as shown in Fig. 1b, due to the widening of the miscibility gap between high-Ca Cpx and Opx with decreasing temperature (e.g., Lindsley et al. 1981). Mass-balance calculations indicate that the CaO and Al_2O_3 contents of experimentally produced pyroxenes are consistent with those from upper mantle peridotite, on the basis of a comparison with a global compilation of Sp lherzolite xenolith compositions (Fig. 2).

Gaetani and Grove (1998) used several lines of evidence to evaluate the approach to equilibrium represented by the experiments analyzed for trace elements in this study. First, experiments were carried out at 1.6 GPa using mixtures of hydrous glass and either a peridotite composition synthesized from oxides or minerals separated from a spinel lherzolite xenolith. The use of different synthetic peridotites means that the minerals in one experiment crystallized from the hydrous glass and synthetic oxide mix starting materials, whereas those in the other equilibrated through exchange with the melt, as well as through the growth of new crystalline material. In this way, the final experimental run product was approached from two, different starting points. There is good agreement between the compositions of the crystalline phases in the two experiments. Second, mass-balance calculations were used to demonstrate that constant sample bulk composition was maintained in the experiments, and average Fe/Mg exchange coefficient ($K_D^{Fe/Mg} = D_{Fe}^{Mineral/Melt}/D_{Mg}^{Mineral/Melt}$) values for Oliv ($0.34 \pm 0.01$ versus 0.33 ± 0.03), Cpx (0.33 ± 0.02 versus 0.36 ± 0.04), Opx (0.32 ± 0.02 versus 0.33 ± 0.04), Sp (0.60 ± 0.13 versus 0.54 ± 0.06), and Gt (0.61 ± 0.03 versus 0.54 ± 0.06) are in agreement with those from the longer duration (18 to 112 h, with a mean duration of 66 h), anhydrous experiments of Kinzler (1997).

The mineral/melt partition coefficients for trace elements determined in this study are reported in Table 1 and shown graphically in Fig. 3 (Cpx/melt), Fig. 4 (Cpx/melt for Na as a function of pressure), and Fig. 5 (Gt/melt). The large-ion-lithophile elements, B, and the light REEs are strongly incompatible with respect to Cpx ($D_K^{Cpx/melt} = 0.0013 \pm 0.0003$ to $D_{Ce}^{Cpx/melt} = 0.16 \pm 0.05$), whereas Ti, Y, and the heavy REEs are moderately incompatible ($D_{Ti}^{Cpx/melt} = 0.32 \pm 0.01$ to $D_{Er}^{Cpx/Melt} = 0.72 \pm 0.34$). There is agreement between Cpx/melt partition coefficients determined in the high- and low-H_2O experiments, with the exception of K which is significantly more incompatible in the former ($D_K^{Cpx/melt} = 0.0013 \pm 0.0003$ versus 0.009 ± 0.002).

A comparison of results from this study with those from the literature show that Cpx/melt partition coeffi-

**Table 3** Electron microprobe analyses of run products from experiments

Expt	Phase	n	SiO₂	TiO₂	Al₂O₃	Cr₂O₃	FeO*	MnO	MgO	CaO	Na₂O	K₂O	P₂O₅	H₂O	Total
B287	Gl	10	46.9(2)	0.66(3)	17.90(10)	0.07(2)	8.41(1)	0.12(4)	11.41(11)	10.71(6)	2.50(11)	0.12(1)	0.13(2)	0.98(24)	99.91
	Cpx	15	51.7(6)	0.25(5)	8.4(9)	0.44(5)	4.8(2)	0.14(2)	19.9(8)	15.0(7)	0.56(3)	–	–	–	101.19
	Opx	10	53.8(7)	0.12(3)	7.3(12)	0.35(6)	6.75(7)	0.13(2)	30.4(4)	2.08(7)	0.10(2)	–	–	–	101.03
	Oliv	7	40.3(3)	0.02(2)	0.13(4)	0.09(3)	11.25(12)	0.12(2)	48.3(3)	0.27(2)	–	–	–	–	100.48
	Sp	3	0.58(2)	0.08(3)	62.7(2)	4.64(9)	8.6(2)	0.09(0)	23.97(5)	0.08(2)	–	–	–	–	100.74
B329	Gl	10	44.78(13)	0.63(2)	17.99(11)	0.08(3)	7.21(13)	0.14(2)	9.39(11)	9.80(8)	2.31(13)	0.12(1)	0.08(2)	6.26(10)	98.79
	Cpx	15	51.4(3)	0.22(3)	7.1(5)	0.31(6)	3.9(2)	0.09(4)	17.5(4)	19.3(4)	0.51(3)	–	–	–	100.33
	Opx	10	54.1(7)	0.10(2)	6.5(7)	0.42(4)	7.41(7)	0.18(2)	30.5(3)	1.35(6)	0.06(1)	–	–	–	100.62
	Oliv	7	40.3(1)	0.00(1)	0.06(2)	0.12(2)	12.2(1)	0.15(3)	47.3(2)	0.17(2)	–	–	–	–	100.30
	Sp	5	0.3(3)	0.12(2)	63.0(5)	4.2(8)	10.0(2)	0.09(1)	22.5(2)	0.3(2)	–	–	–	–	100.51
B394	Gl	10	46.3(2)	0.60(3)	17.08(14)	0.18(3)	8.62(8)	0.16(4)	12.99(12)	10.66(8)	2.22(5)	0.12(1)	0.14(2)	1.70(17)	100.77
	Cpx	15	51.5(5)	0.20(4)	8.7(6)	0.31(3)	4.6(2)	0.11(3)	20.6(4)	13.9(4)	0.63(3)	–	–	–	100.55
	Opx	10	54.1(4)	0.12(3)	7.4(6)	0.35(2)	6.30(8)	0.11(3)	30.6(4)	2.13(3)	0.12(1)	–	–	–	101.23
	Oliv	6	40.2(3)	0.11(1)	0.03(8)	0.14(2)	10.41(7)	0.10(3)	49.5(2)	0.29(2)	–	–	–	–	100.78
	Sp	2	0.38(3)	0.14(1)	64.2(5)	2.93(11)	7.92(11)	0.10(3)	25.0(2)	0.07(0)	–	–	–	–	100.74
B366	Gl	10	44.2(3)	0.66(3)	16.82(9)	0.12(2)	7.77(8)	0.13(3)	11.43(12)	9.86(13)	2.42(12)	0.11(2)	0.16(2)	4.8(6)	98.48
	Cpx	15	51.6(5)	0.19(6)	7.1(10)	0.32(7)	4.1(1)	0.06(5)	18.2(4)	18.4(4)	0.45(3)	–	–	–	100.42
	Opx	10	54.5(8)	0.03(6)	6.1(7)	0.3(1)	7.0(3)	0.10(5)	30.7(10)	1.8(10)	0.07(3)	–	–	–	100.60
	Oliv	7	40.3(2)	0.06(4)	0.04(3)	0.04(2)	11.7(2)	0.13(2)	48.3(2)	0.17(4)	–	–	–	–	100.74
	Gt	9	41.8(2)	0.18(5)	23.3(2)	0.7(1)	8.3(1)	0.32(4)	18.6(2)	6.8(2)	0.02(2)	–	–	–	100.02

All analyses are from Gaetani and Grove (1998), with the exception of the H₂O content of the glass in B394. *N* indicates number of individual electron microprobe analyses used to calculate mean. Units in parentheses, as in Table 1

cients for the REEs are systematically, although not significantly, larger in our experiments, whereas the partition coefficients for Na and Li are significantly smaller (Fig. 3). The variation in the Cpx/melt partition

Fig. 1 a Plot of weight concentrations of SiO₂ versus FeO + MgO, comparing the compositions of experimentally produced low-H₂O (*closed circles*) and high-H₂O (*open circles*) silicate melts saturated with a spinel lherzolite mineral assemblage at 1.2 GPa (Gaetani and Grove 1998). Trace element partition coefficients presented in this study were determined from experiments B287 and B329 (labeled). Uncertainties are 1σ based on replicate electron microprobe analyses. **b** Pseudoternary projection from Sp onto the Oliv–Cpx–SiO₂ plane showing the compositions of coexisting high- and low-Ca pyroxenes which crystallized at 1.2 GPa from silicate melts containing 6.26 ± 0.10 wt% H₂O at 1,185 °C (*open circles*) and 0.98 ± 0.24 wt% H₂O at 1,315 °C (*closed circles*). The systematic change in pyroxene compositions results from the widening of the Cpx–Opx miscibility gap with decreasing temperature. The projection scheme is from Kinzler (1997)

coefficient for Na shown in Fig. 3 is likely attributable to the experimental conditions at which they were determined, as shown in Fig. 4 (Blundy et al. 1995). Further, Brenan et al. (1998) determined that the exchange coefficient for Li and Na between Cpx and melt $\left(K_D^{Li/Na} = D_{Li}^{Cpx/melt}/D_{Na}^{Cpx/melt}\right)$ is approximately constant at 1.30 ± 0.01, which is consistent with values of 1.5 ± 0.4 and 1.18 ± 0.14 measured in our experiments. Therefore, the difference in the $D_{Li}^{Cpx/melt}$ values determined from our experiments and that measured by Hart and Dunn (1993) may also reflect the influence of pressure and temperature. The data compilation shown in Fig. 3 is not intended to be comprehensive but rather represents a comparison among studies in which partition coefficients were determined for a comparable suite of trace elements. It should be noted that Salters and Longhi (1999) investigated pyroxene-melt partitioning over a broader compositional range, and found corre-
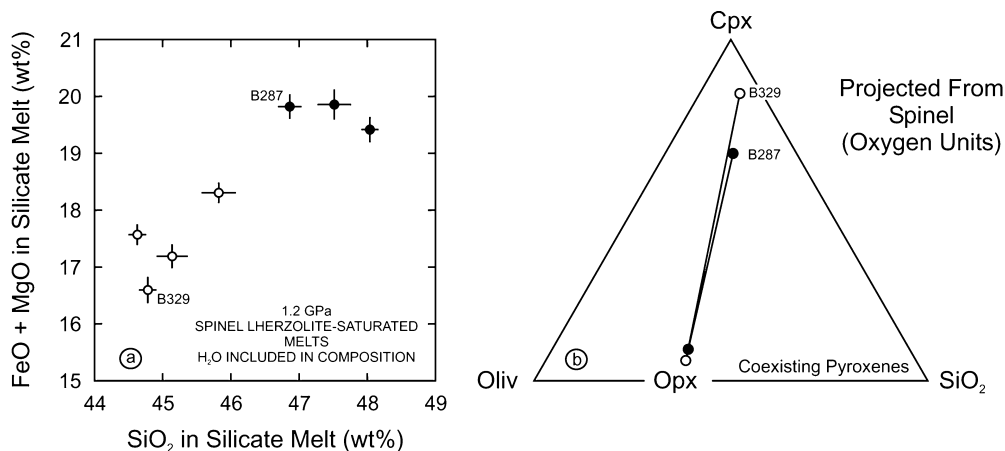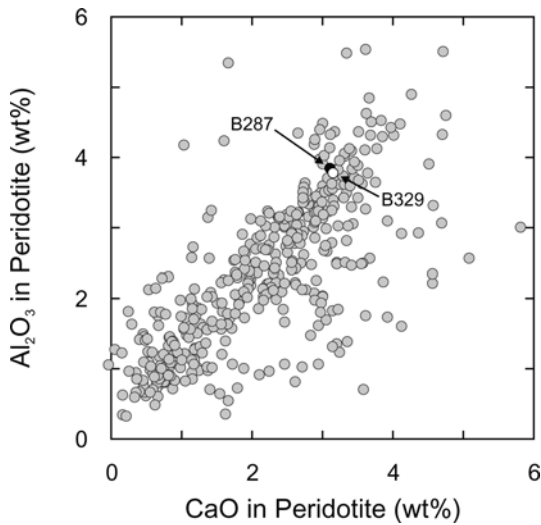
Fig. 2 Plot of weight concentrations of CaO versus Al_2O_3, comparing the compositions of spinel lherzolite xenoliths (*shaded circles*; McDonough 1990 and associated data compilation) with the results from calculations in which the compositions of coexisting Cpx, Opx, Oliv, and Sp from low- (B287; *closed circle*) and high-H_2O (B329; *open circle*) experiments carried out at 1.2 GPa were mass balanced against an estimate for the composition of the oceanic upper mantle (Kinzler 1997). Modes resulting from the calculations are as follows: 15.8 wt% clinopyroxene, 31.6 wt% orthopyroxene, 52.4 wt% olivine, and 0.2 wt% spinel for experiment B287; 13.7 wt% clinopyroxene, 32.3 wt% orthopyroxene, 53.0 wt% olivine, and 1.0 wt% spinel for experiment B329

spondingly greater variability in Cpx/melt partition coefficients, and that Blundy et al. (1998) measured Cpx/melt partition coefficients at 1.5 GPa which are significantly larger than those presented in Fig. 3, especially with respect to the heavy REEs.

Relative compatibilities of trace elements are similar for Gt and Cpx, but the range of Gt/melt partition coefficients is much greater, with K behaving as a strongly incompatible element $\left(D_K^{Cpx/melt} = 0.0006 \pm \right.$ 0.0003$\left.\right)$ and the heavy REEs behaving compatibly $\left(D_{Yb}^{Gt/melt} = 7.4 \pm 1.1\right)$. A comparison of the Gt/melt partition coefficients determined in this study with those from the literature shows that although there is broad agreement, a much wider range of partition coefficients is observed for a given trace element than is the case for Cpx (Figs. 3, 5).

Discussion

Partitioning of trace elements during peridotite melting in the sub-arc mantle

A consensus has emerged that variations in the partitioning of trace elements between minerals and melts are controlled largely by the structure, and, therefore, composition of the crystal (e.g., Beattie 1994; Blundy and Wood 1994). For example, Cpx/melt partition coefficients typically correlate with the concentrations of Ca^{2+} and Al^{3+} in the pyroxene, and this can be interpreted in terms of crystal chemistry (e.g., McKay 1986; Gallahan and Nielsen 1992; Hauri et al. 1994; Lundstrom et al. 1994; Gaetani and Grove 1995; Schosnig and Hoffer 1998; Salters and Longhi 1999; Hill et al. 2000). The dependence of Cpx/melt partition coefficients on Ca^{2+} reflects a variation in the mean size of the M2 site which changes the misfit associated with incorporating large cations into the pyroxene lattice (McKay 1986). The dependence of Cpx/melt partition coefficients on octahedrally and/or tetrahedrally coordinated Al^{3+} is related to charge balance and, therefore, is a function of both the valence state of the substituent cation and the lattice site which it occupies (e.g., Wood and Blundy 2001). Among trace elements which substitute for Ca^{2+} on the M2 site, the partition coefficients for univalent and trivalent cations increase with increasing Al^{3+} in tetrahedral coordination due to the need for local charge

Fig. 3 Spider diagram comparing Cpx/melt partition coefficients determined experimentally in this study (*circles, triangles, squares*) with those determined by Hart and Dunn (1993), Hauri et al. (1994), and Johnson (1998; *shaded symbols*). Error bars are uncertainties from Table 1. The order of elements was chosen primarily to provide a smooth pattern for oceanic basalts (Hofmann 1988; Sun and McDonough 1989). The partition coefficient for B was omitted because its position on the spider diagram is not well determined
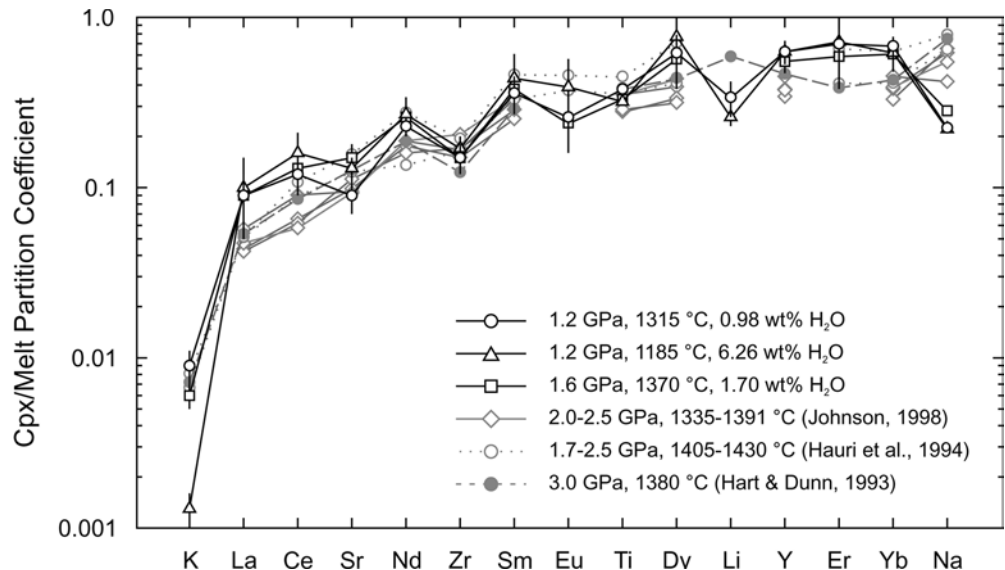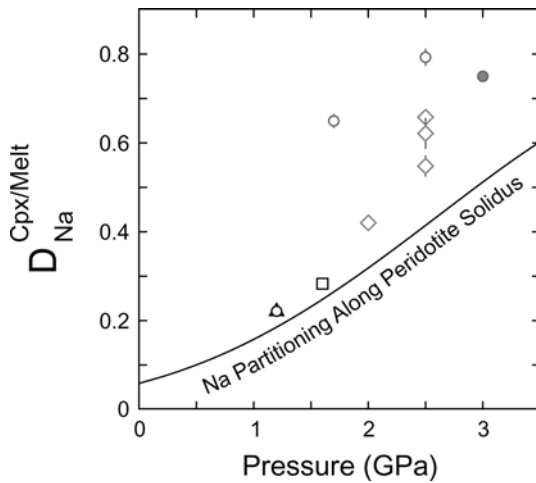
Fig. 4 Plot of pressure versus Cpx/melt partition coefficients for Na, comparing experimentally determined values from this study and the literature (*symbols* are the same as in Fig. 3) with the variation in Na partitioning along the mantle solidus (*curve*) predicted on the basis of Eq. (16) of Blundy et al. (1995) and the parameterization of the peridotite solidus derived by Hirschmann (2000). Note that partition coefficients determined in this study from experiments at 1.2 GPa and temperatures of 1,185 °C (*circle*) and 1,315 °C (*triangle*) plot in the same location

balance, whereas the compatibilities of divalent cations are insensitive to this parameter (Gaetani and Grove 1995; Hill et al. 2000). Among trace elements which substitute for Fe^{2+} and Mg^{2+} on the smaller M1 site, the partition coefficients for tetravalent cations increase as the mean charge associated with the site increases, whereas contraction of the site decreases partition coefficients for divalent and hexavalent cations (Lundstrom et al. 1998; Hill et al. 2000).

In mantle peridotite, Cpx and Opx coexist across a miscibility gap which is sensitive to both temperature and pressure (e.g., Boyd and Schairer 1964; Davis and Boyd 1966; Nehru 1976). In the binary system enstatite–diopside ($Mg_2Si_2O_6$–$CaMgSi_2O_6$), the width of the miscibility gap increases with an isothermal increase in pressure, but decreases as temperature increases at a given pressure (e.g., Lindsley et al. 1981). Therefore, modest variations in pressure–temperature conditions parallel to the anhydrous peridotite solidus are likely to result in correspondingly small variations in the compositions of coexisting pyroxenes. At convergent margins, heat flow from the overlying peridotite into the subducting oceanic lithosphere produces an inverted thermal gradient near the base of the mantle wedge, and thermal models typically predict that temperatures adjacent to the slab are ~800 °C or lower (e.g., Peacock 1991; Davies and Stevenson 1992; Furakawa 1993; Kincaid and Sacks 1997). Therefore, it is expected that Cpx in peridotite at the base of the sub-arc mantle will be more calcic than would be the case at comparable depths beneath an oceanic spreading center. Using the phase relations for the $Mg_2Si_2O_6$–$CaMgSi_2O_6$ binary system at 3.0 GPa determined by Lindsley et al. (1981) as a guide (Fig. 6), the CaO content of coexisting Cpx and Opx are ~16 and ~3 wt%, respectively, at temperatures close to the anhydrous peridotite solidus (~1,500 °C). At temperatures near the amphibole-buffered solidus (~1,100 °C) Cpx contains ~23 wt% CaO and Opx ~1 wt% CaO, whereas at 800 °C the CaO content of Cpx is ~25 wt% and that of Opx ~0.5 wt%. Crystal-chemical changes resulting from these compositional variations should, given the systematics discussed above, result in an increase in Cpx/melt partition coefficients with decreasing temperature for most large cations which substitute for Ca^{2+} on the M2 site.

The pressure and temperature sensitivity of the compositions of coexisting pyroxenes inferred from experiments in the system $Mg_2Si_2O_6$–$CaMgSi_2O_6$ are consistent with the mineral compositions measured in our experiments (Table 3; Fig. 1b). In our low-H_2O

Fig. 5 Spider diagram comparing Gt/melt partition coefficients determined experimentally in this study (*inverted triangles*) with those determined by Hauri et al. (1994) and Johnson (1998) (*shaded symbols*). Error bars are uncertainties from Table 1. The order of elements was chosen primarily to provide a smooth pattern for oceanic basalts (Hofmann 1988; Sun and McDonough 1989). The partition coefficient for B was omitted because its position on the spider diagram is not well determined
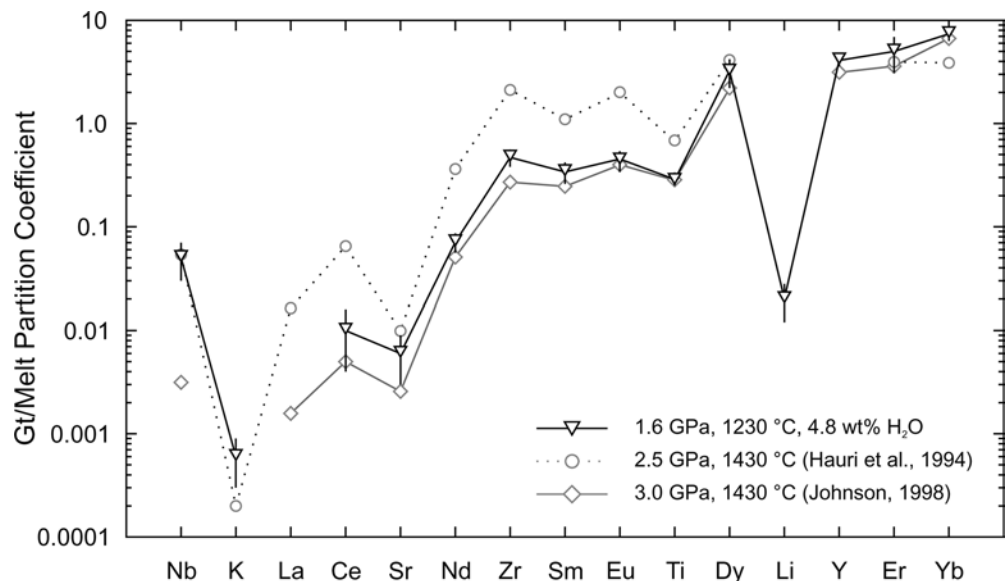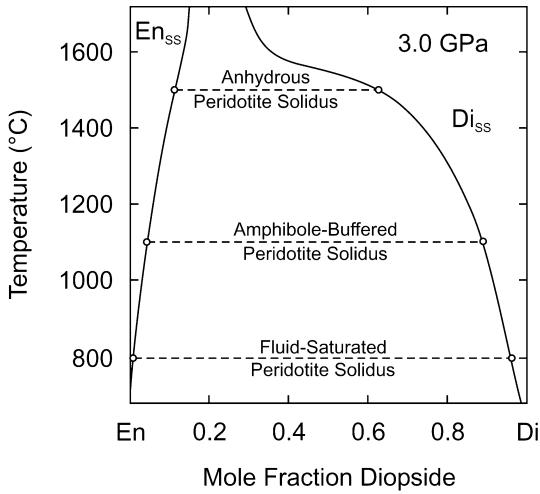
Fig. 6 Temperature–composition diagram showing the miscibility gap separating coexisting Opx and high-Ca Cpx at 3.0 GPa determined experimentally by Lindsley et al. (1981). Shown for reference are the approximate temperatures of the anhydrous, amphibole-buffered, and fluid saturated solidii for upper mantle peridotite at 3.0 GPa

experiments, Cpx and Opx contain 15.0 ± 0.7 wt% and 2.08 ± 0.07 wt% CaO, respectively, at 1.2 GPa and 1,315 °C, whereas at 1.6 GPa and 1,370 °C there is 13.9 ± 0.4 wt% CaO in the Cpx and 2.13 ± 0.03 wt%

Fig. 7a, b Plot of cation radius versus natural logarithm of Cpx/melt partition coefficients (Onuma diagram), showing values determined experimentally for trivalent cations at **a** 1.2 GPa and 1,315 °C, and **b** 1.6 GPa and 1,370 °C. This comparison illustrates the effect on partitioning of increasing temperature and pressure parallel to the peridotite solidus. Also shown are results from weighted nonlinear maximum likelihood fits (Sohn and Menke 2002) to the lattice strain equation of Blundy and Wood (1994; *solid curves*) and partition coefficients predicted on the basis of the compositions of coexisting Cpx and melt using the model of Wood and Blundy (1997; *dashed curves*). The *shaded region* represents uncertainty of predicted values determined by propagating compositional uncertainties using a Monte Carlo simulation. *Vertical dotted lines* show the values of the regression coefficients representing the radii of the M2 crystallographic sites in the experimentally produced pyroxenes. Uncertainties are from Table 1
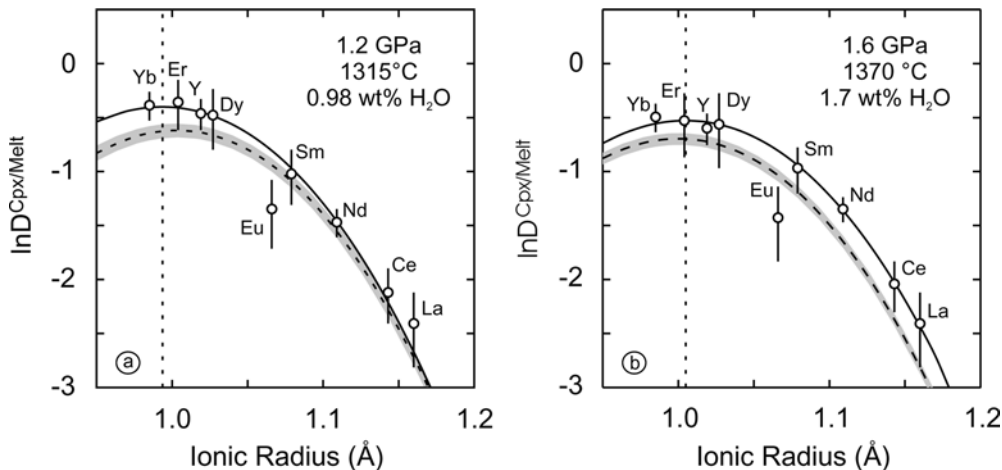
CaO in the Opx. The similarity in pyroxene compositions produced in these two experiments is likely to reflect the balance between the effects of pressure and temperature on the miscibility gap, and should be representative of the magnitude of compositional variations along the peridotite solidus. The parameterization of Hirschmann (2000) predicts that the anhydrous peridotite solidus should increase by 119 °C/GPa between 1.2 (1,273 °C) and 1.6 (1,320 °C) GPa, which is comparable to the temperature change between these two experiments (138 °C/GPa). An isobaric decrease in temperature, enabled by the addition of H_2O, produces a much more significant change in the compositions of coexisting pyroxenes during peridotite partial melting. In the high-H_2O experiment carried out at 1.2 GPa and 1,185 °C, Cpx contains 19.1 ± 0.4 wt% CaO and there is 1.63 ± 0.06 wt% CaO in the Opx. In an experiment carried out at 1,100 °C and 1.2 GPa, Gaetani and Grove (1998) found that Cpx and Opx coexisting with high-H_2O partial melt (dissolved H_2O estimated to be $\sim$12 wt%) contain 20.6 ± 0.4 and 1.2 ± 0.1% CaO, respectively. Conversely, the concentration of Al_2O_3 in Cpx is relatively insensitive to changing the temperature at which partial melting occurs. At 1.2 GPa, Cpx contains 8.4 ± 0.9 wt% Al_2O_3 at 1,315 °C, whereas there is 7.1 ± 0.5 and 7.1 ± 0.7 wt% Al_2O_3 at 1,185 °C and 1,100 °C, respectively. Therefore, on the basis of pyroxene composition, the expectation is that Cpx/melt partition coefficients for most incompatible trace elements which substitute for Ca on the M2 site should be relatively insensitive to changing conditions by 400 MPa parallel to the peridotite solidus, but should increase systematically as the temperature at which hydrous partial melting occurs decreases at a given pressure due to the addition of H_2O.

To test these predictions, Cpx/melt partition coefficients for trivalent cations (REEs and Y) determined in our low-H_2O experiments carried out at 1.2 and 1.6 GPa are compared on Onuma diagrams in Fig. 7, and the two experiments carried out at 1.2 GPa with different amounts of dissolved H_2O are compared in Fig. 8. Partition coefficients for trace elements of a given
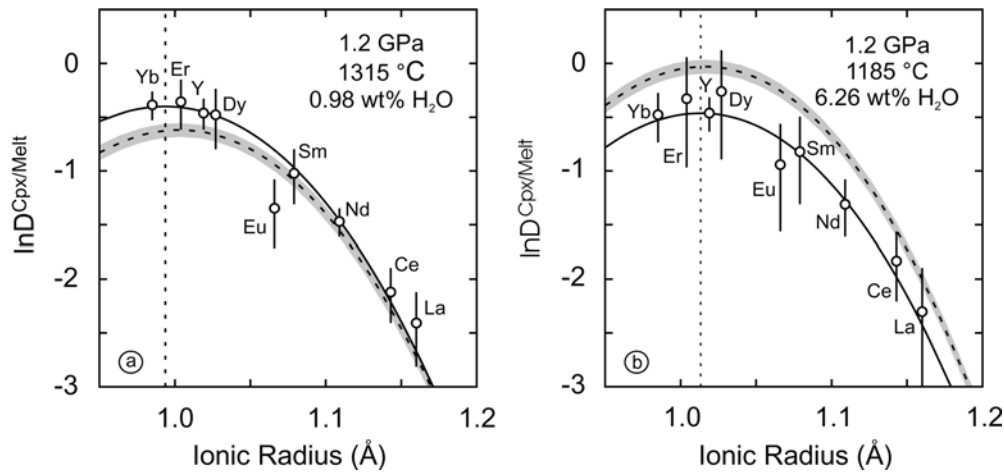
Fig. 8a, b Plot of cation radius versus natural logarithm of Cpx/melt partition coefficients (Onuma diagram), showing values determined experimentally for trivalent cations at **a** 1.2 GPa and 1,315 °C, and **b** 1.2 GPa and 1,185 °C. This comparison illustrates the combined effects on partitioning of increased H_2O and decreased temperature. Also shown are results from weighted nonlinear maximum likelihood fits (Sohn and Menke 2002) to the lattice strain equation of Blundy and Wood (1994; *solid curves*) and partition coefficients predicted on the basis of the compositions of coexisting Cpx and melt using the model of Wood and Blundy (1997; *dashed curves*). The *shaded region* represents uncertainty of predicted values determined by propagating compositional uncertainties using a Monte Carlo simulation. *Vertical dotted lines* represent the values of the regression coefficients representing the radii of the M2 crystallographic sites in the experimentally produced pyroxenes. Uncertainties are from Table 1

valence state substituting onto a single lattice site vary systematically as a function of cationic radius (Onuma et al. 1968). This variability results from the contribution of strain energy, due to the misfit between a substituent cation and the lattice site, to the free energy change for incorporating a cation which fits exactly onto the site (Nagasawa 1966; Brice 1975; Beattie 1994; Blundy and Wood 1994). As the misfit between the optimum radius for the lattice site (r_0) and the radius of the substituent cation (r_i) increases, the mineral/melt partition coefficient $\left(D_i^{mineral/melt}\right)$ decreases according to the equation:

$$D_i^{mineral/melt} = D_0 \exp\left(\frac{-4\pi E N_A \left(\frac{r_0}{2}(r_i - r_0)^2 + \frac{1}{3}(r_i - r_0)^3\right)}{RT}\right)$$

(1)

where D_0 is the mineral/melt partition coefficient for the strain-free substitution, E is the effective Young's modulus for the lattice site, N_A is Avogadro's number, R is the gas constant, and T is temperature (Brice 1975; Blundy and Wood 1994; Wood and Blundy 1997).

Data from our experiments were fit to Eq. (1) in order to quantitatively evaluate how the response of pyroxene crystal-chemistry to changing pressure and temperature conditions affects trace element partitioning (solid curves in Figs. 7 and 8). A comparison of the regression coefficients derived from low-H_2O experi-

ments carried out at 1.2 GPa, 1,315 °C and 1.6 GPa, 1,370 °C indicates that partitioning is not significantly affected by this change in conditions (Table 4). The variation in Cpx composition is relatively minor, so that the values of r_0 derived from the two experiments (0.994 Å at 1.2 GPa; 1.005 Å at 1.6 GPa) are within uncertainty of one another, and the effective Young's modulus for the M2 site does not vary at all (259 GPa for both experiments). The partition coefficient for the strain-free substitution, D_0, decreases slightly from 0.67 at 1.2 GPa to 0.59 at 1.6 GPa. Therefore, the width and position of the parabola represented by Eq. (1) remain essentially constant, and it is translated to slightly lower compatibility.

A comparison of regression coefficients from the low- and high-H_2O experiments carried out at 1.2 GPa indicates that the increased CaO content of the Cpx in the lower-temperature experiment increases the size of the M2 crystallographic site (r_0) from 0.994 Å at 1,315 °C to 1.013 Å at 1,185 °C (Table 4). This has the effect of shifting the maximum REE partition coefficient from Tm (0.994 Å) to Ho (1.015 Å). The effective Young's modulus for the M2 site does not vary significantly (259 versus 263 GPa), so that the width of the parabola represented by Eq. (1) remains nearly constant in going from low-H_2O to high-H_2O conditions. The parabola represented by Eq. (1) retains its shape but is translated to larger cationic radii. The partition coefficient for the strain-free substitution decreases slightly, but not significantly, from 0.67 to 0.63 with increasing H_2O and decreasing temperature. Therefore, our experimental results do not support the prediction that trace elements become systematically more compatible during hydrous peridotite partial melting, demonstrating instead that the cumulative effect of decreasing temperature and increasing dissolved H_2O on Cpx/melt partitioning of the REEs is a relatively minor shift of the compatibility maximum to larger r_i.

For comparison with the regression results, the model of Wood and Blundy (1997), which is calibrated only for anhydrous melt compositions and relies heavily upon crystal chemistry to account for varia-

Table 4 Regression coefficients from fitting partitioning data to the lattice strain equation of Blundy and Wood (1994)

Experiment	Phase	T (°C)	P (GPa)	E (GPa)	r_o (Å)	D_o
Regression results						
B287	Cpx	1,315	1.2	259	0.994	0.67
95% confidence limits				238	0.986	0.63
				275	0.997	0.69
B329	Cpx	1,185	1.2	263	1.013	0.63
95% confidence limits				249	1.007	0.59
				273	1.019	0.68
B394	Cpx	1,370	1.6	259	1.005	0.59
95% confidence limits				234	0.994	0.55
				283	1.015	0.62
Model predictions						
B287	Cpx	1,315	1.2	269	1.003	0.54
95% confidence limits				264	1.002	0.47
				277	1.004	0.61
B329	Cpx	1,185	1.2	274	1.015	0.97
95% confidence limits				272	1.016	0.85
				277	1.017	1.10
B394	Cpx	1,370	1.6	270	1.0000	0.50
95% confidence limits				269	1.0001	0.44
				271	1.0002	0.55

Weighted nonlinear regressions were carried out using the maximum likelihood method (Sohn and Menke 2002)

tions in partitioning, was used to predict the partition coefficients for trivalent trace elements on the basis of the major element compositions of coexisting pyroxene and melt (dashed curve in Figs. 7 and 8; Table 4). There is reasonably good agreement between the model predictions and regression coefficients for both low-H_2O experiments: $r_0 = 1.003$ Å versus 0.994 Å, $E = 269$ GPa versus 259 GPa, and $D_0 = 0.54$ versus 0.67 at 1.2 GPa, 1,315 °C and $r_0 = 1.000$ Å versus 1.005 Å, $E = 270$ GPa versus 259 GPa, and $D_0 = 0.50$ versus 0.59 at 1.6 GPa, 1,370 °C. Further, the model predicts the observed decrease in D_0 as pressure and temperature increase approximately parallel to the peridotite solidus. Overall, the model predicts Cpx/melt partition coefficients for both the heavy REEs (e.g., $D_{Yb}^{CPx/melt} = 0.53 \pm 0.03$ versus 0.68 ± 0.09) and the light REEs (e.g., $D_{La}^{CPx/melt} = 0.066 \pm 0.004$ versus 0.09 ± 0.03) for the low-H_2O experiments which are slightly smaller than the measured values (Fig. 7). A comparison of the model prediction and regression coefficients for the high-H_2O, 1.2-GPa experiment demonstrates that there is reasonably good agreement with respect to both r_0 (1.016 versus 1.013 Å) and E (274 versus 263 GPa), but that the predicted value for D_0 is higher by a factor of 1.5 (0.97 vs. 0.63). Further, the model predicts that D_0 should increase from 0.54 to 0.97, rather than decrease from 0.67 to 0.63, with decreasing temperature and increasing dissolved H_2O. This discrepancy results in predicted REE partition coefficients which are systematically too high (Fig. 8b). Green et al. (2000) report a similar discrepancy between the predicted and observed values for D_0 from their measurements of REE partitioning between high-Ca Cpx and hydrous quartz tholeiite equilibrated at 2.0 to 3.0 GPa and 1,200 to 1,230 °C.

The prediction from the Wood and Blundy (1997) model that REE partition coefficients should increase with decreasing temperature at 1.2 GPa is, as noted above, based upon data from anhydrous experiments and is heavily reliant upon crystal chemistry to account for variations in compatibility. Predicting partition coefficients from Eq. (1) using the approach of Wood and Blundy (1997) requires calculating (1) r_0 for the M2 site as a function of pyroxene composition, (2) E for the M2 site on the basis of cation valence, temperature, and pressure, and (3) D_0 from an expression which depends upon temperature, pressure, and the compositions of both crystal and melt. That a significant discrepancy exists between the regression results and the model prediction only for D_0 suggests that the mismatch is related to variations in melt structure which are not accounted for in the parameterization used to calculate this variable. The sole melt compositional parameter included in the predictive expression for D_0 (and, therefore, the only measure of melt structure incorporated into the model of Wood and Blundy 1997) is the molar $Mg/(Mg + Fe)$ ratio. Experimental studies of the distribution of trace elements between coexisting immiscible silicate melts demonstrate that, under anhydrous conditions, REEs partition preferentially into liquids with lower SiO_2 contents and higher concentrations of network-modifying cations (Watson 1976; Ryerson and Hess 1978; Ellison and Hess 1989). If, as suggested by these studies, polymerization represents the primary melt-structural control on mineral/melt partition coefficients, an increase in the concentration of dissolved H_2O should lead to decreased compatibility in the solid, thereby explaining the discrepancy in the predicted D_0 value.

There is, at present, no way to rigorously determine the influence of H_2O-related melt structural changes on Cpx/melt partition coefficients. The effect of melt polymerization on partitioning can be quantitatively evaluated for anhydrous systems, however, on the basis of results from the thermal diffusion (Soret effect) experiments of Lesher (1986). When an initially homo-

geneous silicate melt is held in an externally imposed temperature gradient, diffusional mass flow is driven by variations in chemical potential. At steady state, the melt is characterized by a compositional gradient in which network-forming components (e.g., SiO_2) are enriched at the hot end of the thermal diffusion array, and network-modifying components (e.g., FeO, MgO, CaO) are concentrated at the cool end (e.g., Walker et al. 1981; Lesher and Walker 1986). Lesher (1986) exploited this phenomenon to investigate the effects of silicate melt structure on mineral/melt partition coefficients in the portion of composition space relevant to natural magmas, where liquid immiscibility is rare. Experimental Soret fractionation data were used to constrain the influence of melt structure on partition coefficients by calculating trace element concentration ratios as a function of position along the length of the thermal diffusion array according to the expression:

$$M_f^i = \frac{X_i}{X_i(\text{reference})},\tag{2}$$

where $X_i(\text{reference})$ is the concentration of trace element i at one end of the array, and X_i is the concentration of element i at any other point along the array. If, as in the case for immiscible melts, it is assumed that a single crystal composition can be in equilibrium with two different melt compositions along the thermal diffusion array, Eq. (2) can be rewritten as:

$$D_i^{\text{mineral/melt}} = \frac{D_i^{\text{mineral/melt}}(\text{reference})}{M_i^f}.\tag{3}$$

Fig. 9a Plot of M_f^{Ce} versus % network modifiers in the silicate melt, showing a linear regression of results from the Soret diffusion experiments of Lesher (1986). Extrapolation along the regression line was used to estimate the influence of melt structural changes, produced by increasing the H_2O content of the melt from 0.98 ± 0.24 to 6.26 ± 0.10 wt%, on $D_{Ce}^{Cpx/melt}$ (*stars*). **b** Onuma diagram showing the result of applying melt structure correction (*arrows*) determined from Soret diffusion experiments to partition coefficients predicted on the basis of the compositions of coexisting Cpx and melt using the model of Wood and Blundy (1997). *Symbols* and uncertainties are the same as in Fig. 8b
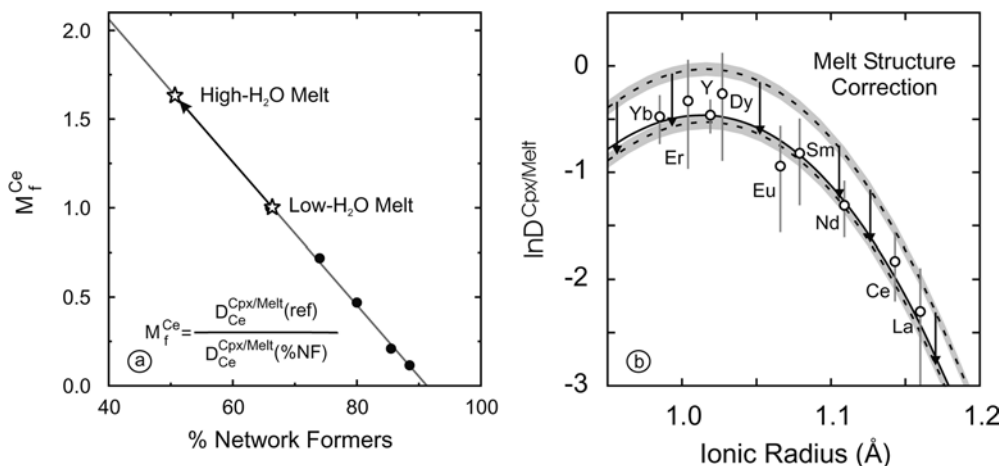
In order to evaluate whether the influence of melt structure is sufficient to account for the discrepancy in D_0 values inferred from our experiments, Soret fractionation data for Ce from the study of Lesher (1986) were used to calculate M_f^{Ce} values. The data define a linear relationship between M_f^{Ce} and % network modifiers (NM) for silicate melts with compositions ranging from 66% NM, at 1,250 °C, to 88.5% NM at 1,510 °C. An extrapolation of this relationship was used to estimate that $D_{Ce}^{Cpx/melt}$ should decrease from 0.12 in the low-H_2O experiment (66.3% NM at 1,315 °C) to 0.07 in the high-H_2O experiment (50.5% NM at 1,185 °C) on the basis of the change in melt polymerization (Fig. 9a). Although this calculation does not specifically account for the effects of dissolved H_2O, it does indicate that the discrepancy in D_0 is consistent with the compatibility change predicted on the basis of melt polymerization. If $D_{Ce}^{Cpx/melt}$ predicted for the high-H_2O experiment by the Wood and Blundy (1997) model (0.21) is "corrected" for the change in melt polymerization on the basis of results from the Soret experiments, the calculated partition coefficient (0.13) is nearly identical to the fit of our data to Eq. (1) (0.14), bringing the model prediction into close agreement with the regression results (Fig. 9b). Therefore, it is probable that the similarity in $D_i^{Cpx/melt}$ values measured in the high- and low-H_2O experiments reflects a balance between the change in mineral structure, which tends to increase Cpx/melt partition coefficients, and the variation in melt structure, which acts to decrease them.

There are several potential explanations for the agreement between the Wood and Blundy (1997) model for partitioning in anhydrous systems and our experimental results for melts containing ~1–2 wt% H_2O. First, it is possible that the concentration of hydroxyl groups is not large enough to significantly affect the structure of the melt. We investigated this possibility by quantitatively estimating the concentrations of molecular H_2O and hydroxyl groups in our experimentally produced melts, using the temperature dependence of the equilibrium constant for H_2O speciation:

$$K_{eq} = \frac{\left(a_{OH}^{melt}\right)^2}{a_O^{melt} a_{H_2O}^{melt}} \qquad (4)$$

determined by Ihinger et al. (1999) for rhyolites containing less than 2.5 wt% total H_2O (Fig. 10). Although this calculation involves significant extrapolation, the temperature dependence of H_2O speciation for basaltic melts is unknown and existing data indicate that speciation in basaltic and albitic glasses are comparable (Dixon et al. 1995). Results from these calculations suggest that our low-H_2O melts contain ~4–6 mol% hydroxyl groups, which is enough to decrease viscosity by ~60% relative to an anhydrous melt at the same temperature (Shaw 1972). For comparison, the addition of 6.26 wt% H_2O produces ~17 mol% hydroxyl groups and decreases viscosity by ~98% relative to an anhydrous melt at the same temperature. Therefore, it is likely that the presence of ~1–2 wt% H_2O has an influence on melt structure and trace element partitioning. A more likely explanation for the agreement between model prediction and experimental result is that the high-pressure experiments which represent a significant proportion of the calibration of the Wood and Bundy (1997) model contain melts with ~1–2 wt% dissolved H_2O, due to the difficulty involved in drying out the powders used as starting materials. Because the solubility of H_2O in silicate melts is only ~1,000 ppm at 0.1 MPa, this would imply that the pressure dependence for D_0 implicitly includes the effect of increasing the concentration of dissolved H_2O.

Partitioning of trace elements during melting of "damp" mantle peridotite

It is probable that H_2O plays a role in partial melting of mantle peridotite in most tectonic environments.
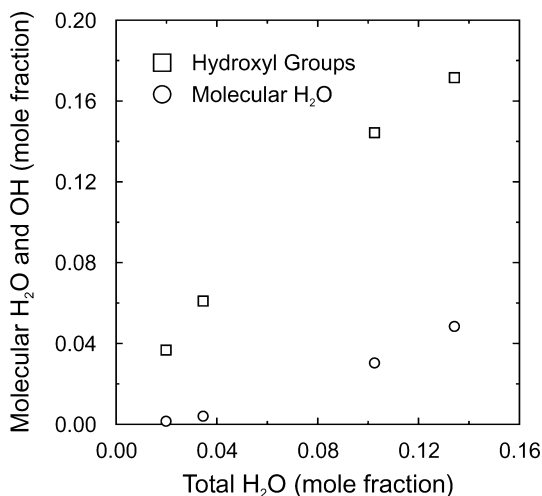
The presence of H_2O dissolved in mantle minerals beneath oceanic ridges and plume-related oceanic islands is thought to initiate melting along an H_2O-undersaturated, or "damp", solidus, dehydrating the residual peridotite (Plank and Langmuir 1992; Hirth and Kohlstedt 1996; Kinzler 1997; Ito et al. 1999; Braun et al. 2000). In contrast with the case of the sub-arc mantle discussed above, partial melting of damp peridotite in response to adiabatic decompression of the oceanic upper mantle takes place at temperatures *higher* than those associated with the anhydrous peridotite solidus along a given isentrope. For example, based on the solidii used by Hirth and Kohlstedt (1996), anhydrous peridotite with a potential temperature of 1,350 °C begins to melt at 2.0 GPa and 1,390 °C, whereas peridotite containing ~100–200 ppm H_2O will cross the solidus at 3.7 GPa and 1,425 °C. Hydrous partial melts produced at these conditions are expected have low SiO_2 (e.g., Kawamoto and Holloway 1997), and to be in equilibrium with a single, CaO- and Al_2O_3-poor clinopyroxene (Fig. 11), coexisting on the peridotite solidus with Gt and Oliv (Takahashi 1986; Takahashi et al. 1993; Walter 1998). As noted above, decreasing the CaO content of the Cpx tends to lower $D_i^{Cpx/melt}$ values, as does decreasing the degree of polymerization of the silicate melt. Therefore, the combination of deploymerized melt and sub-calcic Cpx at the "damp" solidus should lower partition coefficients during the earliest stages of melting beneath oceanic ridges and plume-related oceanic islands. It is difficult to predict, however, whether these partition coefficients would be significantly different from those along the anhydrous solidus at pressures near the Sp-to-Gt transition, where anhydrous melting is thought to start (e.g., Salters and Longhi 1999).

Fig. 10 Plot of the mole fractions of water dissolved in quenched basaltic glasses as molecular H_2O (*circles*) and as hydroxyl groups (*squares*) versus total water content of the glass calculated using an ideal solution model and speciation data determined from rhyolitic glasses (Stolper 1982; Ihinger et al. 1999)
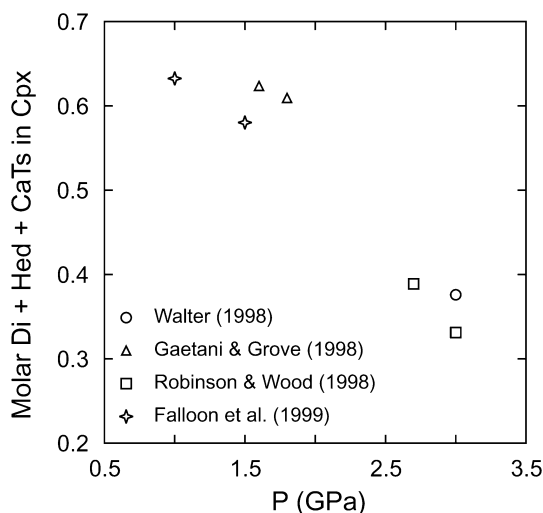

Fig. 11 Plot comparing the compositions of Cpx produced experimentally at or near the peridotite solidus at pressures of 1.0 to 3.0 GPa from the studies of Walter (1998), Gaetani and Grove (1998), Robinson and Wood (1998), and Falloon et al. (1999)

403

Conclusions

An experimental determination of the partitioning of incompatible trace elements between high-Ca Cpx and silicate melts containing up to 6.3 wt% dissolved H_2O at upper mantle conditions demonstrates that most trace elements are not as compatible under hydrous conditions as would be predicted on the basis of Cpx composition. This result indicates that the low degree of polymerization of hydrous partial melts measurably affects trace element partitioning. Models designed to predict the partitioning of trace elements between Cpx and anhydrous silicate melt cannot be used to model melt generation under hydrous conditions without taking into account the affect of melt structure on trace element partitioning.

References

Akella J, Kennedy GC (1971) Melting of gold, silver, and copper—Proposal for a new high-pressure calibration scale. J Geophys Res 76:4969–4977

Arculus RJ, Johnson RW (1981) Island arc magma sources: a geochemical assessment of the roles of slab-derived components and crustal contamination. Geochem J 15:109–133

Ayers JC, Eggler DH (1995) Partitioning of elements between silicate melt and H_2O-NaCl fluids at 1.5 and 2.0 GPa pressure: implications for mantle metasomatism. Geochim Cosmochim Acta 59:4237–4246

Ayers JC, Dittmer SK, Layne GD (1997) Partitioning of elements between peridotite and H_2O at 2.0–3.0 GPa and 900–1100 °C, and applications to models of subduction zone processes. Earth Planet Sci Lett 150:381–398

Beattie P (1994) Systematics and energetics of trace-element partitioning between olivine and silicate melts: implications for the nature of mineral/melt partitioning. Chem Geol 117:57–71

Blundy JD, Wood BJ (1994) Prediction of crystal-melt partition coefficients from elastic moduli. Nature 372:452–454

Blundy JD, Falloon TJ, Wood BJ, Dalton JA (1995) Sodium partitioning between clinopyroxene and silicate melts. J Geophys Res 100:15501–15515

Blundy JD, Robinson JAC, Wood BJ (1998) Heavy REE are compatible in clinopyroxene on the spinel lherzolite solidus. Earth Planet Sci Lett 160:493–504

Boyd FR, England JL (1960) Apparatus for phase equilibrium studies at pressures up to 50 kbar and temperatures up to 1750 °C. J Geophys Res 65:741–748

Boyd FR, Schairer JF (1964) The system $MgSiO_3$-$CaMgSi_2O_6$. J Petrol 5:275–309

Braun MG, Hirth JG, Parmentier EM (2000) The effects of deep damp melting on mantle flow and melt generation beneath mid-ocean ridges. Earth Planet Sci Lett 176:339–356

Brenan JM, Watson EB (1991) Partitioning of trace elements between olivine and aqueous fluids at high P-T conditions: implications for the effect of fluid composition on trace element transport. Earth Planet Sci Lett 107:672–688

Brenan JM, Shaw HF, Phinney DL, Ryerson FJ (1994) Rutile-aqueous fluid partitioning of Nb, Ta, Hf, Zr, U and Th: implications for high field strength element depletions in island-arc basalts. Earth Planet Sci Lett 128:327–339

Brenan JM, Shaw HF, Ryerson FJ (1995a) Experimental evidence for the origin of lead enrichment in convergent-margin magmas. Nature 378:54–56

Brenan JM, Shaw HF, Ryerson FJ, Phinney DL (1995b) Mineral-aqueous fluid partitioning of trace elements at 900 °C and 2.0 GPa: constraints on the trace element chemistry of mantle and deep crustal fluids. Geochim Cosmochim Acta 59:3331–3350

Brenan JM, Neroda E, Lundstrom CC, Shaw HF, Ryerson FJ, Phinney DL (1998) Behaviour of boron, beryllium, and lithium during melting and crystallization: constraints from mineral-melt partitioning experiments. Geochim Cosmochim Acta 62:2129–2141

Brice JC (1975) Some thermodynamic aspects of the growth of strained crystals. J Crystal Growth 28:249–253

Davies JH, Stevenson DJ (1992) Physical model of source region of subduction zone volcanics. J Geophys Res 97:2037–2070

Davis BTC, Boyd FR (1966) The join $Mg_2Si_2O_6$-$CaMgSi_2O_6$ at 30 kilobars pressure and its application to pyroxenes from kimberlites. J Geophys Res 71:3567–3576

Dixon JE, Clague DA, Stolper EM (1991) Degassing history of water, sulfur, and carbon in submarine lavas from Kilauea Volcano, Hawaii. J Geol 99:371–394

Dixon JE, Stolper EM, Holloway JR (1995) An experimental study of water and carbon dioxide solubilities in mid-ocean ridge basaltic liquids. Part I: calibration and solubility models. J Petrol 36:1607–1631

Ellison AJG, Hess PC (1989) Solution properties of rare earth elements in silicate melts: inferences from immiscible liquids. Geochim Cosmochim Acta 53:1965–1974

Fahey AJ, Goswami JN, McKeegan KD, Zinner E (1987) [26]Al, [244]Pu, [50]Ti, REE, and trace element abundances in hibonite grains from CM and CV meteorites. Geochim Cosmochim Acta 52:329–350

Falloon TJ, Green DH, Danyushevsky LV, Faul UH (1999) Peridotite melting at 1.0 and 1.5 GPa: an experimental evaluation of techniques using diamond aggregates and mineral mixes for determination of near-solidus melts. J Petrol 40:1343–1375

Furakawa Y (1993) Magmatic processes under arcs and formation of the volcanic front. J Geophys Res 98:8309–8319

Gaetani GA (1996) Experimental investigations of differentiation processes in the terrestrial planets. PhD Dissertation, Massachusetts Institute of Technology

Gaetani GA, Grove TL (1995) Partitioning of rare earth elements between clinopyroxene and silicate melt: crystal chemical controls. Geochim Cosmochim Acta 59:1951–1962

Gaetani GA, Grove TL (1998) The influence of water on melting of mantle peridotite. Contrib Mineral Petrol 131:323–346

Gallahan WE, Nielsen RL (1992) The partitioning of Sc, Y, and the rare earth elements between high-Ca pyroxene and natural mafic to intermediate lavas at 1 atmosphere. Geochim Cosmochim Acta 56:2387–2404

Gill JB (1981) Orogenic andesites and plate tectonics. Springer, Berlin Heidelberg New York

Govindaraju K (1989) 1989 compilation of working values and sample description for 272 geostandards. Geostand Newslett 13:113

Green TH, Blundy JD, Adam J, Yaxley GM (2000) SIMS determination of trace element partition coefficients between garnet, clinopyroxene and hydrous basaltic liquids at 2–7.5 GPa and 1080–1200 °C. Lithos 53:165–187

Hart SR, Dunn T (1993) Experimental cpx/melt partitioning of 24 trace elements. Contrib Mineral Petrol 113:1–8

Hauri EH, Wagner TP, Grove TL (1994) Experimental and natural partitioning of Th, U, Pb, and other trace elements between garnet, clinopyroxene, and basaltic melts. Chem Geol 117:149–166

Hauri EH, Wang J, Dixon JE, King PL, Mandeville C, Newman S (2002) SIMS analysis of volatiles in silicate glasses 1. Calibration, matrix effects and comparisons with FTIR. Chem Geol 183:99–114

Hays JF (1966) Lime-alumina-silica. Carnegie Inst Washington Yearb 65:234–239

Hill E, Wood BJ, Blundy JD (2000) The effect of Ca-Tschermaks component on trace element partitioning between clinopyroxene and silicate melt. Lithos 53:203–215

Hirschmann MM (2000) Mantle solidus: experimental constraints and the effects of peridotite composition. Geochem Geophys Geosyst 1. DOI 10.1029/2000GC000070

Hirth JG, Kohlstedt DL (1996) Water in the oceanic upper mantle: implications for rheology, melt extraction and the evolution of the lithosphere. Earth Planet Sci Lett 144:93–108

Hofmann AW (1988) Chemical differentiation of the Earth: the relationship between mantle, continental crust, and oceanic crust. Earth Planet Sci Lett 90:297–314

Ihinger PD, Zhang Y, Stolper EM (1999) The speciation of dissolved H_2O in rhyolitic melt. Geochim Cosmochim Acta 63:3567–3578

Ito G, Shen Y, Hirth JG, Wolfe CJ (1999) Mantle flow, melting, and dehydration of the Iceland mantle plume. Earth Planet Sci Lett 165:81–96

Johnson KTM (1998) Experimental determination of partition coefficients for rare earth and high-field strength elements between clinopyroxene, garnet, and basaltic melt at high pressures. Contrib Mineral Petrol 133:60–68

Johnson MC, Plank T (1999) Dehydration and melting experiments constrain the fate of subducted sediments. Geochem Geophys Geosyst 1. DOI 10.1029/1999GC000014

Kawamoto T, Holloway JR (1997) Melting temperature and partial melt chemistry of H_2O-saturated mantle peridotite to 11 Gigapascals. Science 276:240–243

Kennedy AK, Hutcheon ID (1992) Chemical and isotopic constraints on the formation and crystallization of SA-1, a basaltic Allende plagioclase-olivine inclusion. Meteoritics 27:539–559

Kent AJR, Norman MD, Hutcheon ID, Stolper EM (1999) Sea water assimilation in an oceanic volcano: evidence from matrix glasses and glass inclusions from Loihi seamount, Hawaii. Chem Geol 156:299–319

Kincaid C, Sacks IS (1997) Thermal and dynamical evolution of the upper mantle in subduction zones. J Geophys Res 102:12295–12315

Kinzler RJ (1997) Melting of mantle peridotite at pressures approaching the spinel to garnet transisiton: application to mid-ocean ridge basalt petrogenesis. J Geophys Res 102:853–874

Lesher CE (1986) Effects of silicate liquid composition on mineral-liquid element partitioning from Soret diffusion studies. J Geophys Res 91:6123–6141

Lesher CE, Walker D (1986) Solution properties of silicate liquids from thermal diffusion experiments. Geochim Cosmochim Acta 50:1397–1411

Lindsley DH, Grover JE, Davidson PM (1981) The thermodynamics of the $Mg_2Si_2O_6$-$CaMgSi_2O_6$ join: a review and an improved model. In: Newton RC, Navrotsky A, Wood BJ (eds) Thermodynamics of minerals and melts. Springer, Berlin Heidelberg New York, pp 149–175

Lundstrom CC, Shaw HF, Ryerson FJ, Phinney DL, Gill JB, Williams Q (1994) Compositional controls on the partitioning of U, Th, Ba, Pb, Sr, and Zr between clinopyroxene and haplobasaltic melts: implications for uranium series disequilibria in basalts. Earth Planet Sci Lett 128:407–423

Lundstrom CC, Shaw HF, Ryerson FJ, Williams Q, Gill JB (1998) Crystal chemical control of clinopyroxene-melt partitioning in the Di-Ab-An system: implications for elemental fractionations

in the depleted mantle. Geochim Cosmochim Acta 62:2849–2862

Maury RC, Defant MJ, Joron J-L (1992) Metasomatism of the sub-arc mantle inferred from trace elements in Philippine xenoliths. Nature 360:661–663

McDonough WF (1990) Constraints on the composition of the continental lithospheric mantle. Earth Planet Sci Lett 101:1–18

McKay G (1986) Clinopyroxene REE distribution coefficients for shergottites: the REE content of the Shergotty melt. Geochim Cosmochim Acta 50:927–937

Nagasawa H (1966) Trace element partition coefficient in ionic crystals. Science 152:767–769

Nehru CE (1976) Pressure dependence of the enstatite limb of the enstatite-diopside solidus. Am Mineral 61:578–581

Onuma N, Higuchi H, Wakita H, Nagasawa H (1968) Trace element partition between two pyroxenes and the host lava. Earth Planet Sci Lett 5:47–51

Peacock SM (1991) Numerical simulation of subduction zone pressure-temperature-time paths: constraints on fluid production and arc magmatism. Philos Trans R Soc Lond Ser A 335:341–353

Perfit MR, Gust DA, Bence AE, Arculus RJ, Taylor SR (1980) Chemical characteristics of island-arc basalts: implications for mantle sources. Chem Geol 30:227–256

Plank T, Langmuir CH (1992) Effects of melting regime on the composition of the oceanic crust. J Geophys Res 97:19749–19770

Presnall DC, Hoover JD (1987) High pressure phase equilibrium constraints on the origin of mid-ocean ridge basalts. In: Mysen BO (ed) Magmatic processes: physiochemical principles. Geochem Soc Spec Publ 1:75–89

Robinson JAC, Wood BJ (1998) The depth of the spinel to garnet transition at the peridotite solidus. Earth Planet Sci Lett 164:277–284

Ryerson FJ, Hess PC (1978) Implications of liquid-liquid distribution coefficients to mineral-liquid partitioning. Geochim Cosmochim Acta 42:921–932

Salters VJM, Longhi J (1999) Trace element partitioning during the initial stages of melting beneath mid-ocean ridges. Earth Planet Sci Lett 166:15–30

Schneider ME, Eggler DH (1986) Fluids in equilibrium with peridotite minerals: implications for mantle metasomatism. Geochim Cosmochim Acta 50:711–724

Schosnig M, Hoffer E (1998) Compositional dependence of REE partitioning between diopside and melt at 1 atmosphere. Contrib Mineral Petrol 133:205–216

Shaw HR (1972) Viscosities of magmatic silicate liquids: an empirical method of prediction. Am J Sci 272:870–893

Sisson TW, Grove TL (1993) Experimental investigations of the role of H_2O in calc-alkaline differentiation and subduction zone magmatism. Contrib Mineral Petrol 113:143–166

Sohn RA, Menke W (2002) Application of maximum likelihood and bootstrap methods to nonlinear curve-fit problems in geochemistry. Geochem Geophys Geosyst 3. DOI 10.1029/2001GC000253

Stolper EM (1982) The speciation of water in silicate melts. Geochim Cosmochim Acta 46:2609–2620

Stolper EM, Newman S (1994) The role of water in the petrogenesis of Mariana trough magmas. Earth Planet Sci Lett 121:293–325

Sun S-S, McDonough WF (1989) Chemical and isotopic systematics of oceanic basalts: implications for mantle composition and processes. In: Saunders AD, Norry MJ (eds) Magmatism in the ocean basins. Geol Soc Spec Publ 42:313–345

Takahashi E (1986) Melting of dry peridotite KLB-1 up to 14 GPa: implications on the origin of peridotitic upper mantle. J Geophys Res 91:9367–9382

Takahashi E, Shimazaki T, Tsuzaki Y, Yoshida H (1993) Melting study of a peridotite KLB-1 to 6.5 GPa, and the origin of basaltic magmas. Philos Trans R Soc Lond Ser A 342:105–120

Tatsumi Y, Hamilton DL, Nesbitt RW (1986) Chemical characteristics of fluid phase released from a subducted lithosphere

and origin of arc magmas: evidence from high-pressure experiments and natural rocks. J Volcanol Geotherm Res 29:293–309

Walker D, Lesher CE, Hays JF (1981) Soret separation of lunar liquid. Proc Lunar Planet Sci Conf 12:991–999

Walter MJ (1998) Melting of garnet peridotite and the origin of komatiite and depleted lithosphere. J Petrol 39:29–60

Watson EB (1976) Two-liquid partition coefficients: experimental data and geochemical implications. Contrib Mineral Petrol 56:119–134

Wood BJ, Blundy JD (1997) A predictive model for rare earth element partitioning between clinopyroxene and anhydrous silicate melt. Contrib Mineral Petrol 129:166–181

Wood BJ, Blundy JD (2001) The effect of cation charge on crystal-melt partitioning of trace elements. Earth Planet Sci Lett 188:59–71

Wyllie PJ (1982) Subduction products according to experimental prediction. Geol Soc Am Bull 93:468–476

Zinner E, Crozaz G (1986) A method for the quantitative measurement of rare earth elements on the ion microprobe. Int J Mass Spectrom Ion Proc 69:17–38